Materials Today Bio 16 (2022) 100433

Contents lists available at ScienceDirect

Materials Today Bio

journal homepage: www.journals.elsevier.com/materials-today-bio

The combination of a 3D-Printed porous Ti–6Al–4V alloy scaffold and stem cell sheet technology for the construction of biomimetic engineered bone at an ectopic site

Zhifa Wang [a,1], Leng Han [b,1], Ye Zhou [c,1], Jiacheng Cai [a], Shuohui Sun [a], Junli Ma [a], Weijian Wang [a,***], Xiao Li [a,**], Limin Ma [d,*]

[a] Department of Stomatology, General Hospital of Southern Theater of PLA, Guangzhou, 510010, China
[b] Department of Pathology, General Hospital of Southern Theater of PLA, Guangzhou, 510010, China
[c] Laboratory of Basic Medicine, General Hospital of Southern Theater of PLA, Guangzhou, 510010, China
[d] Department of Orthopedics, Guangdong Provincial People's Hospital, Guangdong Academy of Medical Sciences, Guangzhou, 510080, China

ARTICLE INFO

Keywords:
Cell sheet technology
3D-printed porous titanium alloy scaffold
Osteogenesis
Angiogenesis
Biomimetic engineered bone

ABSTRACT

Cell sheet technology has been widely used in bone tissue engineering and regenerative medicine. However, controlling the shape and volume of large pieces of engineered bone tissue remains impossible without additional suitable scaffolds. Three-dimensional (3D) printed titanium (Ti) alloy scaffolds are mostly used as implant materials for repairing bone defects, but the unsatisfactory bioactivities of traditional Ti-based scaffolds severely limit their clinical applications. Herein, we hypothesize that the combination of bone marrow mesenchymal stem cell (BMSC) sheet technology and 3D porous Ti–6Al–4V (PT) alloy scaffolds could be used to fabricate biomimetic engineered bone. First, various concentrations of BMSCs were directly cocultured with PT scaffolds to obtain complexes of osteoblastic cell sheets and scaffolds. Then, as an experimental control, an osteoblastic BMSC sheet was prepared by continuous culturing under osteogenic conditions for 2 weeks without passaging and used to wrap the scaffolds. The BMSC sheet was composed of several layers of extracellular matrix (ECM) and a mass of BMSCs. The BMSCs exhibited excellent adherent, proliferative and osteogenic potential when cocultured with PT scaffolds, which may be attributed to the ability of the 3D microstructure of scaffolds to facilitate the biological behaviors of cells, as confirmed by the in vitro results. Moreover, the presence of BMSCs and ECM increased the angiogenic potential of PT scaffolds by the secretion of VEGF. Micro-CT and histological analysis confirmed the in vivo formation of biomimetic engineered bone when the complex of cocultured BMSCs and PT scaffolds and the scaffolds wrapped by prepared BMSC sheets were implanted subcutaneously into nude mice. Therefore, the combination of BMSC sheet technology and 3D-printed PT scaffolds could be used to construct customized biomimetic engineered bone, offering a novel and promising strategy for the precise repair of bone defects.

1. Introduction

The repair of bone defects in the oral maxillofacial region and limbs caused by severe trauma, malignant tumors that commonly need to be resected surgically, and innate diseases such as congenital bilateral maxillary absence remains a great challenge and a crucial clinical issue [1,2]. After all the research performed in the past decades, bone grafts remain the gold standard for bone repair despite the accompanying donor morbidity and related issues, including the time and cost of surgery [3,4]. Allografts and xenografts obviously have some advantages, such as abundant sources and the lack of size limitations, but the risks of immunological rejection and potential infection with exogenous pathogens make them impossible to use widely in the clinic [5–7]. Fortunately, advances in bone tissue engineering by stem cell-based approaches, mostly bone marrow mesenchymal stem cells (BMSCs) and adipose-derived stem cells (ADSCs), offer a promising strategy for the reconstruction of bone defects [2,8].

* Corresponding author.
** Corresponding author.
*** Corresponding author.
E-mail addresses: wwei7182@163.com (W. Wang), drlixiao@163.com (X. Li), malimin7@126.com (L. Ma).
[1] The authors contributed equally to this work and should be considered co-first authors.

https://doi.org/10.1016/j.mtbio.2022.100433
Received 20 July 2022; Received in revised form 12 September 2022; Accepted 14 September 2022
Available online 15 September 2022

Previous studies suggested that implanting autologous bone marrow via injection was a useful and convenient strategy for the treatment of bone nonunion and spinal cord injury regeneration [9,10]. However, a large portion of the stem cells in implanted bone marrow were dissociated and difficult to retain at the initial transplant site, and the number of stem cells and progenitor cells in bone marrow is low [11]. To obtain a sufficient number of stem cells, the cells needed have to be cultured and expanded for several passages in vitro, which inevitably decreases cell viability and leads to the loss of cell–cell connections and extracellular matrix (ECM), which are essential for cell proliferation and differentiation, because of repeated treatments with trypsin. In addition, physical or mechanical damage during cell passaging, harvesting, and injection may also be harmful to cell viability [2,11]. A mass of biomaterials, including hyaluronate, collagen, alginate, and fibrin, have been introduced into bone regeneration as cell carriers to modify the retention of dissociated stem cells and to offer cells an appropriate matrix for bone formation [12,13]. However, shortcomings such as the potential toxicity of degradation products, possible immunogenicity, unstable degradation rate, and unpredictable cell-scaffold interactions make these scaffolds far from satisfactory, let alone ideal [14]. Cell sheet technology, including the culture of primary or passage 2 stem cells to form sheets and retain intact cell-ECM interactions and cell–cell connections, has been confirmed to be useful for the regeneration of several tissues, such as bone, cartilage, liver and heart [15–17]. Furthermore, the cell sheet was easily obtained using a cell scraper without the need for digestion with trypsin, was flexible and could easily wrap various shapes of biomaterials or deposits within the porous scaffolds, and could be made thicker by stacking several layers of cell sheets [11,18,19].

Due to the poor mechanical strength of cell sheets, however, they cannot be used to reconstruct or repair large bone defects [2]. Millions of titanium alloy implants (such as Ti–6Al–4V and TC4), which are characterized by biosafety, appropriate mechanical strength, mature processing techniques, and the good corrosion resistance of TC4, have been implanted in bone defect restoration and joint replacement surgeries every year [20–22]. However, TC4 implants, such as the Ti reconstruction plates used in the surgical repair of maxillectomy and mandibulectomy, retain the problems of bone nonunion, bone resorption, plate exposure, a limited life span, and the discrepant rigidity between the host bone and Ti alloy scaffolds, although they have been widely used in the clinic for decades [23]. To solve the aforementioned problems, various approaches have been introduced into the surface modification of TC4 implants [24]. Chemotactic factors were seeded within the scaffolds to perfect the 3D microstructure, thus facilitating the ingrowth of bone tissue [25,26]. Gelatin methacrylate (GelMA) hybrid scaffolds were proven to be able to increase the osseointegration of TC4 materials. In addition, a GelMA hybrid TC4 porous scaffold with dual bionic features (GMPT) was designed and prepared to mimic the porous and interconnected structure of natural bone, which promoted the inner growth of newly formed vessels and bone tissues [27,28]. Unfortunately, the intrinsic inertness of TC4 impedes the interaction between scaffolds and osteogenesis-related cells, such as BMSCs [29]. Thus, a pillowy GelMA hydrogel matrix was used to mimic the natural ECM of bone to improve the interaction of osteogenesis-related cells with GMPT, which achieved somewhat satisfactory results [28]. The natural ECM has sustainable and dynamic interactions with the surrounding cells and sequentially exerts essential effects on the bioactivities of cells, such as proliferation, migration, and differentiation, in the process of tissue regeneration and organ formation [30,31]. However, exogenous or synthetic matrix substitutes fail to perfectly mimic the natural ECM, especially in terms of releasing cytokines and functioning in tissue regeneration [32].

In this research, we hypothesize that the combination of BMSC sheet technology and 3D porous Ti–6Al–4V (PT) scaffolds could be used for the fabrication of biomimetic engineered bone. First, different concentrations of BMSCs were directly cocultured with PT scaffolds to obtain complexes of osteoblastic cell sheets and scaffolds. Then, an osteoblastic BMSC sheet was formed by continuous culturing under osteogenic conditions for 2 weeks without passaging and used to wrap the scaffolds as an experimental control. BMSCs showed excellent adherent, proliferative and osteogenic potential when cocultured with PT, which may be attributed to the 3D microstructure of scaffolds facilitating the biological behaviors of cells, as confirmed by the in vitro results. Moreover, the presence of BMSCs and ECM also increased the angiogenic potential of PT scaffolds. Finally, cocultured complexes of BMSCs and PT scaffolds and scaffolds wrapped by prepared BMSC sheets were also implanted subcutaneously into nude mice, and the in vivo formation of biomimetic engineered bone was evaluated by micro-CT and histological analysis.

2. Materials and methods

2.1. Ethical approval for animal experiments

This study was examined and authorized by the Institutional Animal Care and Use Committee of the General Hospital of Southern Theater of PLA, Guangzhou, China (No. 2021121001). A total of six male 4-week-old young immature New Zealand white rabbits and twenty-seven severe combined immunodeficiency (SCID) mice were used in this study.

2.2. Preparation of 3D-printed porous Ti–6Al–4V alloy scaffolds

According to our previous study, 3D-printed porous Ti–6Al–4V alloy scaffolds were prepared with minor modifications [21]. In detail, a Selective Laser Melting (SLM) 3D printer (Concept Laser M2, Upper Franconia, Germany) equipped with an Yb fiber laser with a focus beam 50 μm in diameter was selected to fabricate Ti–6Al–4V powder (Sandvik, Sweden) with a diameter of 15–50 μm into porous Ti–6Al–4V (PT) alloy scaffolds. The SLM fabrication process was performed under a specified Ar/N2 atmosphere using a laser (100 W) based on a certain battery of scanning terms (layer, 50 μm thick; rate, 650 mm/s; separation, 70 μm). The PT scaffolds were prepared in a cylindrical form with a diameter of 12 mm and a thickness of 2 mm. Then, 75% alcohol and deionized water were used to rinse the prepared PT scaffolds under continuous physical agitation (200 rpm on an orbital shaker) 3 times, followed by disinfection by ultraviolet radiation for 30 min. The fabricated PT scaffolds were collected for further application.

2.3. Isolation of BMSCs and formation of osteoblastic cell sheets

A total of six male 4-week-old New Zealand white rabbits were selected and sacrificed via the intraperitoneal injection of an overdose of chloral hydrate to harvest bone marrow mesenchymal stem cells (BMSCs), in line with the method described previously [2,33]. In brief, after the rabbits were immersed in 75% alcohol for 30 min to disinfect, the iliac bone and limb long bone were obtained from the rabbits and cleaned 3 times for 5 min each with phosphate-buffered saline (PBS) containing streptomycin (100 μg/ml) and penicillin (200 U/ml) (Amresco, USA); next, the marrow in the iliac bone and limb long bone was rinsed out with Dulbecco's Modified Eagle's Medium-F12 (DMEM-F12; HyClone, Logan, Utah, USA) containing 10% fetal bovine serum (FBS, HyClone), streptomycin (100 μg/ml) and penicillin (200 U/ml). The collected cell clusters were pipetted and dispersed to acquire a suspension of bone marrow cells. The obtained cell suspensions were then seeded in a 100-mm petri dish at a concentration of 5×10^4 cells/cm^2. On the third and seventh days after cell plating, all of the floating cells were discarded. The remaining adherent cells were passaged, allowed to reach 90%–95% confluence, and then plated in 100-mm petri dishes at a concentration of 5×10^4 cells/cm^2 and cultured. A portion of the passage 2 cells was used for further experiments, and the other portion of the cells was used to form cell sheets. Briefly, the cells were resuspended and seeded in 6-well plates at a concentration of 5×10^4 cells/cm^2, and the medium was changed to high-glucose DMEM containing 20% fetal bovine serum (FBS, HyClone), streptomycin (100 μg/ml), penicillin (200 U/ml), 272 μg/ml L-glutamine

(Amresco), 50 mg/ml L-ascorbic acid 2-phosphate, 100 nM dexamethasone, 272 μg/ml L-glutamine and 10 mM β-glycerophosphate (Sigma), which was also termed the osteogenic medium. After 2 weeks of continuous culturing without passaging, the formed cell sheet could be lifted effortlessly with a cell scraper and collected for histological analysis, microstructural observation, and further experiments. Moreover, to decrease the potential individual differences in BMSCs obtained from various rabbits, BMSCs from six donors were collected and mixed together for osteogenic cell sheet preparation and further experiments.

2.4. Direct coculture of the BMSCs and 3D PT scaffolds

To investigate the optimal cell concentration for seeding on 3D PT scaffolds to form cell sheet, a direct coculture assay of BMSCs and PT scaffolds was performed in accordance with the procedures described previously [21]. In detail, a total of 5 groups were established in this experiment: (1) blank control group: PT scaffolds with no cell seeding (PT), (2) low cell seeding number group: PT scaffolds with cell seeding at 5×10^3 cells/cm^2 (PT/LC, PT/low cell seeding), (3) medial cell seeding number group: PT scaffolds with cell seeding at 5×10^4 cells/cm^2 (PT/MC, PT/medial seeding cell), (4) high cell seeding number group: PT scaffolds with cell seeding at 5×10^5 cells/cm^2 (PT/HC, PT/high seeding cell), and (5) experimental control group: one piece of formed cell sheet in six-well plates wrapped PT scaffolds (PT/CS, PT/prepared cell sheet). Briefly, 200 μL of passage 2 BMSC suspension containing various numbers of cells based on the aforementioned groups was seeded into PT scaffolds plated in six-well plates. After incubation for 1 h to allow cells to migrate into the PT scaffolds and further reach preliminary adherence, 10 ml of osteogenic medium was added to the plates to culture the cells.

2.5. Observation of cell viability, attachment, and proliferation

To investigate the viability, attachment, and proliferation capacity of BMSCs on PT scaffolds in osteogenic medium, different concentrations of cells according to the previous grouping were plated with the PT scaffolds. After coculturing for 24 h, a live/dead test was performed to measure the cell viability. Moreover, FITC phalloidin and DAPI were used to stain the cytoskeleton and cell nuclei, respectively, and then the cells seeded on the PT scaffolds were fixed for cell morphology analysis, followed by observation via confocal laser microscopy (CLSM, Leica, Japan). Then, a cell counting kit-8 (CCK-8) was used to assess the proliferative capacity of BMSCs at the seventh and fourteen days after seeding in line with a previously published method with minor modification [34]. Next, after the cultured cells were processed according to the reported protocols, scanning electronic microscopy (SEM) (S-4800, Hitachi, Japan) observation was performed to investigate the detailed morphology of the BMSCs and the formation of ECM derived from BMSCs on PT scaffolds.

2.6. Osteogenesis examination

On the seventh and fourteen days after coculture of BMSCs and PT scaffolds under osteogenic conditions, alizarin red (AR) staining and alkaline phosphate (ALP) staining were used according to the manufacturer's protocol to assess the matrix mineralization and the osteogenic potential of BMSCs, respectively [35]. Both qualitative observation and quantitative comparison were performed in these assays.

Furthermore, quantitative real-time PCR (RT–PCR) based on the primers listed in Table 1 was carried out to assess the mRNA levels of the genes related to osteogenesis on days 7 and 14 of coculturing following the manufacturer's directions. In detail, the expression of osteogenesis-related genes in BMSCs, including osteocalcin (OCN), osteopontin (OPN), collagen I (COL-I), and runt-related transcription factor 2 (Runx2), was investigated by RT–PCR. Briefly, total cellular RNA was isolated using the Total RNA Kit (Omega Bio-Tek, GA, USA), and its quality was determined using a NanoDrop 2000/2000c spectrophotometer (Thermo Fisher Scientific, MA, USA) at 260/280 nm, followed by reverse transcription into cDNA utilizing the PrimeScript™ RT Reagent Kit Perfect Real Time (TaKaRa Biotechnology, Dalian, China). Next, the levels of mRNA were tested using Premix Ex Taq™ (TaKaRa, China) in an ABI 7500 Real-Time PCR Cycler (Applied Biosystems, CA, USA). The $2^{-\Delta\Delta}$CT method was used to study the relative expression levels.

Table 1
Gene primer sequences for RT–PCR of BMSCs.

Genes	Primer Sequences	PCR Product (bp)
OCN	Forward 5′-CTACCAGCGCTTCTACGG-3′ Reverse 5′-TCCTCTTCTGGAGTTTATTGGG-3′	88
OPN	Forward 5′-TCCAAAGTCAGCCAGGAATC-3′ Reverse 5′-GTCTGTGCTCTTCATCCTCTTC-3′	97
COL-I	Forward 5′-CCTTGCCTGCTTCCTGTAAA-3′ Reverse 5′-CTGGGTTGTTTGTCGTCTGT-3′	99
Runx2	Forward 5′-CAAGTAGCCACCTATCACAGAG-3′ Reverse 5′-GGCGGTCAGAGAACAAACTA-3′	112
β-actin	Forward 5′-GGCCGAGGACTTTGATTGTA-3′ Reverse 5′-TCACATGGCATCTCACGATATT-3′	78

In addition, western blotting (WB) was used to analyze the expression of osteogenesis-related proteins, including OCN, OPN, COL-I, and Runx2. In brief, RIPA cell lysis buffer was used to isolate proteins from BMSCs and cell sheets. The concentrations of collected proteins were calculated using the Bradford protein assay kit (Bio-Rad). Then, SDS–PAGE gels were utilized to separate proteins, followed by transfer to a polyvinylidene difluoride membrane that was blocked with 5% skimmed milk in Tris-buffered saline/Tween-20 (TBST). Primary antibodies, including *anti*-OCN (Genetex, 1:1000), *anti*-OPN (Novusbio, 1:1000), anti-COL-I (Bioss, 1:1000), *anti*-Runx2 (Bioss, 1:1000), and *anti*-β-actin (Abcam, 1:1000), were added to the membranes. After incubation overnight at 4 °C, secondary antibodies (anti-rabbit IgG) were added and allowed to react for half an hour at room temperature. The chemiluminescence of the blots was analyzed by using ECL Western blotting substrate (Pierce). In addition, to diminish variability, all of the RT–PCR and WB tests were carried out three times.

2.7. Angiogenesis evaluation

Human umbilical vein endothelial cells (HUVECs) of passages 3–5 used in this experiment were obtained from ScienCell (USA). After 24 h of coculture of PT scaffolds and BMSC/BMSC sheets, the supernatant was collected, named conditioned medium derived from BMSCs (BMSC-CM), and used to culture HUVECs to perform angiogenesis assays, such as wound healing and tube formation assays [36]. First, a wound healing assay was utilized to assess the migration capacity of HUVECs cultured in BMSC-CM. In detail, HUVECs were resuspended in BMSC-CM and seeded in six-well plates at 6×10^5 cells/well, then incubated at 37 °C for 24 h until the cells reached approximately 90%–95% confluence. Then, the tip of a 200 μL pipette was used to scratch the cell monolayers vertically, followed by gentle washing three times with PBS and continued culture in serum-free medium. At 0, 12, and 24 h after scratching, a white light microscope was used to capture images with 6 fields per well. The quantitative wound healing rate (final area/initial area) was measured using ImageJ software.

For the tube formation assay, the Matrigel basement membrane matrix (Corning Inc, Corning, NY, USA) was plated in a 96-well plate precooled on ice on ice at 50 μL/well, followed by incubation at 37 °C for half an hour to solidify the Matrigel. Then, HUVECs were added to 96-well plates at a density of 1×10^3 cells/well, and tube formation was evaluated 4 h after cell seeding. The images were captured and analyzed quantitatively using AngioTool software. Moreover, after HUVECs were cultured in BMSC-CM for 24 h, FITC phalloidin and CD31 immunofluorescence staining were used to stain the cytoskeleton and endothelial cells, respectively. After the cells were fixed to study cell morphology, a

confocal laser microscope (CLSM, Leica, Japan) was used to capture images.

In addition, quantitative real-time PCR (RT–PCR) based on the primers itemized in Table 2 was performed to evaluate the mRNA level of angiogenesis-related genes at 24 h of culturing with BMSC-CM. Specifically, the angiogenesis-related genes expressed by HUVECs, including vascular endothelial growth factor (VEGF) and basic fibroblast growth factor (bFGF), were investigated by RT–PCR. Furthermore, WB was used to analyze the expression of angiogenesis-related proteins, including VEGF and bFGF. The technical processes were similar to those described for RT–PCR and WB.

2.8. In vivo transplantation assay

To further evaluate the osteogenic and angiogenic potential of the PT scaffolds cocultured with BMSCs under osteogenic conditions or PT wrapped by a prepared osteogenic BMSC sheet in vivo, a heterotopic transplantation assay was performed in SCID mice. A total of 24 transplantation sites on 24 6-week-old male mice were randomly classified into three groups (n = 8 in each group): PT scaffolds cocultured with low cell seeding (PT/LC group, cell seeding at 5×10^3 cells/cm^2); PT scaffolds cocultured with high cell seeding (PT/HC group, cell seeding at 5×10^5 cells/cm^2); and PT scaffolds wrapped by an osteogenic BMSC sheet (PT/CS group). In each group, 4 implants were implanted into the left side, and the other 4 implants were implanted on the right side. After the mice were anesthetized with 3% isoflurane gas, a 1 cm longitudinal incision was made parallel to the spine on the left or right dorsal skin of the mice, followed by blunt separation, and materials were transplanted into the subcutaneous sites. Finally, the wound was closed with a 5–0 absorbable suture. The remaining 3 mice served as a positive control for evaluating the biocompatibility and biosafety of PT scaffolds in vivo. Postoperatively, all the nude mice were housed in cages and allowed to move freely immediately after surgery, no painkillers were administrated to the nude mice after surgery, and all wounds healed well without any evidence of infection or wound dehiscence.

2.9. Microcomputed tomography (micro-CT) and histological analysis

At 12 weeks after transplantation, the mice were sacrificed, and the samples were harvested, collected and scanned with a Micro-CT instrument (Latheta, Tokyo, Japan) to examine the formation of new bone. In detail, the scanning parameters were set at 40 μA and 80 kV at 48 μm resolution. On the basis of the CT data, the area of the PT scaffolds was considered the region of interest (ROI). To quantitatively assess newly regenerated bone in the scaffolds, bone volume/tissue volume (BV/TV) was measured using VG Studio MAX software. After the collected samples were fixed in 10% formalin and dehydrated with ethanol (70%, 80%, 90%, 95%, and 100%), they were embedded, processed, and sectioned at 35 μm thickness, stained with Masson's trichrome (MTC), and finally observed by a light microscope (DX51, Olympus, Tokyo, Japan). In addition, histomorphometric examinations were performed to compare the newly formed mineralized bone and cartilage (blue staining) among different groups as reported previously with a minor modification [2]. Furthermore, CD31 immunofluorescence staining was carried out to evaluate angiogenesis in vivo. In detail, 3% bovine serum albumin (BSA) was used to block tissue slices, followed by incubation with anti-CD31 primary antibody (Abcam, USA, 1:500) at 4 °C overnight. Then, DAPI was added to observe the nuclei. Finally, a fluorescence microscope (Olympus, Japan) was used to capture the views.

Table 2
Gene primer sequences for RT–PCR of HUVECs.

Genes	Primer Sequences	PCR Product (bp)
VEGF	Forward 5′-CAGGACATTGCTGTGCTTTG-3′ Reverse 5′-CTCAGAAGCAGGTGAGAGTAAG-3′	122
bFGF	Forward 5′-GCAGTGGCTCATGCCTATATT-3′ Reverse 5′-GGTTTCACCAGGTTGGTCTT-3′	92
β-actin	Forward 5′-GGCCGAGGACTTTGATTGTA-3′ Reverse 5′-TCACATGGCATCTCACGATATT-3′	78

2.10. Statistical analysis

All of the data were collected from at least three parallel samples in vitro or eight samples in vivo and are presented as the mean ± standard deviation (SD). Statistical differences were analyzed using ANOVA via GraphPad Prism 6.0 software, and statistical significance was accepted at $^*p < 0.05$.

3. Results and discussion

3.1. Adhesion, proliferation, and viability of BMSCs on PT scaffolds

As regard to 3D printed porous titanium (PT) alloy scaffolds, this scaffolds used in this study had a magnitude stress of 47 MPa, along with a Young's modulus of 1.60 ± 0.4 GPa and with a porosity of 75% [21]. As shown in Fig S1, BMSCs grew well when cocultured with PT scaffolds, and a large amount of ECM adhered to the surface of the scaffolds (Fig S1D, yellow arrow). The cell toxicity of PT scaffolds was evaluated by the live/dead assay. Fig S2 shows that BMSCs had excellent cellular growth behavior, and few dead cells were observed, indicating the good cytocompatibility and biosafety of the PT scaffolds. After 14 days of coculture of BMSCs and PT scaffolds in osteogenic induction medium, FITC (fluorescein isothiocyanate)-phalloidin staining showed that the largest amount of F-actin, an ideal component for observing the cytoskeleton, appeared in BMSCs in the PT/HC and PT/CS groups compared to the others (Fig. 1N and O). Moreover, more cytoskeleton appeared as the number of initial inoculated cells was increased (Fig. 1K-N), suggesting better cell adhesion capacity in the PT/HC and PT/CS groups. To investigate cell adhesion on PT scaffolds when BMSCs were cultured in osteogenic induction medium, which could facilitate the formation and deposition of extracellular matrix (ECM) secreted by BMSCs and thus allow BMSCs to embed in the ECM and facilitate cell sheet formation, SEM was used to observe the morphology of BMSCs and the formation of their autocrine ECM (Fig S3A-E). In detail, no cells or ECM was observed in the PT group (Fig. 1P and U). In the PT/LC group, a few cells adhered to the surface of PT scaffolds (Fig. 1Q, red arrow), and almost no ECM was deposited around the BMSCs (Fig. 1V). In contrast, in the PT/HC group, a large number of BMSCs adhered to the surface and inner sides of the scaffolds (Fig. 1S, yellow arrow and blue arrow, respectively) and were embedded in the abundant secreted ECM. In the PT/MC group, more cells adhered than in the PT/LC group, and a small amount of ECM was observed on the surface of the scaffolds (Fig. 1R, green arrow). Osteoblastic cell sheets were observed in the PT/CS group (Fig. 1T and Fig S3E), where a cell sheet was made up of the cells (Fig. 1Y, red pentacle) and their secreted ECM (Fig. 1Y, black arrow). Moreover, EDS spectra showed that the surface elemental components of PT/CS were C, O, Ti, Al, and V (Fig S3O), whereas the PT scaffolds were mainly composed of Ti, Al, and V (Fig S3K). A CCK-8 assay was used to assess the proliferative potential of BMSCs on PT scaffolds, as shown in Fig. 1Z, on days 7 and 14. At both detection times, there was no significant difference between the PT/HC group and the PT/CS group, and both values were significantly higher than those of the PT/MC and PT/LC groups ($p < 0.05$). In summary, 3D microstructure of PT scaffolds facilitate the biological behaviors of BMSCs about adherent, proliferative and osteogenic potential. The aforementioned results suggested that PT/HC and PT/CS could be considered the better combinations for the growth and proliferation of BMSCs and the formation of ECM, consequently offering a desirable microenvironment for tissue regeneration [30].

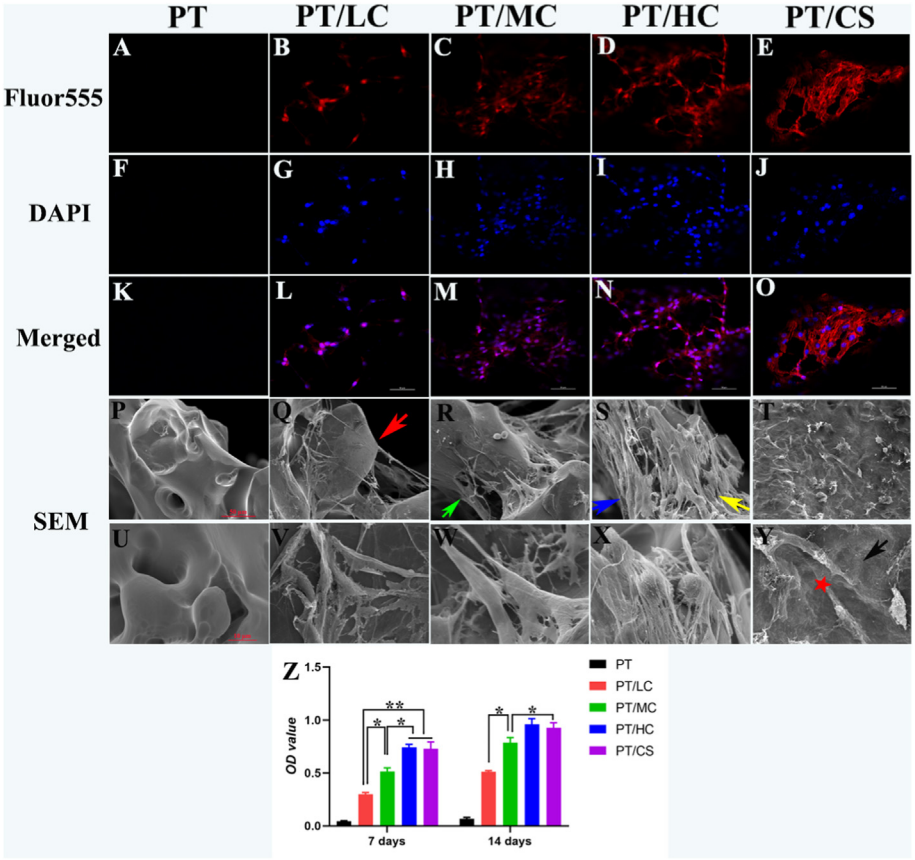

Fig. 1. In vitro adhesion, proliferation, and viability of BMSCs on PT scaffolds. (A–O) Phalloidin-DAPI staining of BMSCs attached to PT. Scale bar = 50 μm. In detail, (A–E) FITC phalloidin was used to stain the cytoskeleton. (F–J) DAPI was used to stain cell nuclei. (K–O) Merged views of the cytoskeleton and cell nuclei. (P–Y) SEM of BMSCs attached to PT. (P–T) Low-magnification SEM images show the adhesion and proliferation of BMSCs on PT scaffolds. In the PT/LC group, a few cells adhered to the surface of the PT scaffolds (Q, red arrow). In the PT/MC group, more cells adhered than in the PT/LC group, and a small amount of ECM was observed on the surface of the scaffolds (R, green arrow). In contrast, in the PT/HC group, a large number of BMSCs adhered to the surface and inner sides of scaffolds (S, yellow arrow and blue arrow, respectively) and were embedded in their abundant secreted ECM. (U–Y) High-magnification SEM images show the adhesion and proliferation of BMSCs on PT scaffolds. An osteoblastic cell sheet was observed in the PT/CS group (T), made up of cells (Y, red pentacle) and their secreted ECM (Y, black arrow). (Z) CCK-8 assay of BMSCs on PT on days 7 and 14. * indicates significant differences ($p < 0.05$).

3.2. Osteogenesis of the combination of BMSCs and PT scaffolds

Several assays were performed to investigate the optimal cell concentration for seeding on PT scaffolds and to determine the best combination for osteogenesis (Fig. 2A). First, Alizarin red staining and ALP staining were chosen to evaluate the mineralization and osteogenic potential of BMSCs on PT scaffolds, respectively, under osteogenic induction conditions. At the seventh and fourteen days of coculturing, the PT group had the lowest staining compared with the PT/LC, PT/MC, PT/HC, and PT/CS groups; meanwhile, the best staining and some small pieces of cell sheet fragments were observed in the PT/HC and PT/CS groups (Fig. 2B), which was also verified by SEM examination (Fig S2 A-J). The quantification of Alizarin red staining based on the relative absorbance values substantiated these observations. Both qualitative and quantitative results proved that more matrix mineralization occurred in the PT/HC and PT/CS groups, and there was no significant difference between them at either time point (days 7 and 14) (Fig. 2C). However, greater staining and higher quantification were observed as the number of initial seeding cells increased ($p < 0.05$). Moreover, the prolongation of coculturing time, from seven days to fourteen days, also increased the staining and quantitative expression (Fig. 2C). In addition, the activity of ALP in the PT/HC and PT/CS groups was obviously higher than that in the other groups on the seventh and fourteen days, and there was no significant difference between the PT/HC and PT/CS groups (Fig S3). Interestingly, the PT/MC group had higher ALP activity than the PT/LC group on day 14 ($p < 0.05$, Fig S4). These results demonstrated that increasing the initial number of seeding cells improved the osteogenic potential of BMSCs on PT scaffolds because ECM mineralization and ALP activity expression, typical markers of osteogenic differentiation of BMSCs in the late and early stages, were obviously increased, which was consistent with previous publications [28,37]. In particular, the PT/HC and PT/CS groups had optimal osteogenic differentiation results at 7 and 14 days.

To further verify the abovementioned results, RT–PCR and Western blotting (WB) were used to test the expression levels of osteogenesis-related genes and proteins, including OCN, OPN, COL-I, and Runx2. After 7 and 14 days of coculturing, the mRNA expression levels of OCN, OPN, COL-I, and Runx2 in the PT/HC and PT/CS groups were markedly higher than those in the other groups ($p < 0.05$) (Fig. 2D–G). There was no significant difference between the PT/HC and PT/CS groups ($p > 0.05$). Specifically, the levels of OPN and Runx2 in the PT/MC group were higher than those in the PT/LC group on day 14 ($p < 0.05$), indicating that increasing the number of initial seeding cells favored the capability of osteogenic differentiation (Fig. 2E and G). The WB analysis presented results similar to those of RT–PCR (Fig. 2H). Consistent with the qualitative and quantitative results of Alizarin red and ALP activity staining, the PT/HC and PT/CS groups exhibited the best osteogenic differentiation, with significantly upregulated osteogenesis-related gene and protein expression compared with the other PT groups (Fig. 2B–H and Fig S4).

3.3. Angiogenesis of the combination of BMSCs and PT scaffolds

Angiogenesis plays a vital role in bone regeneration by providing sufficient nutrition and bioactive cues and enabling the excretion of metabolic waste components [25,38]. The angiogenic capability of BMSCs has been confirmed and used for the revascularization of ischemic heart tissue in the clinic, and BMSCs were proven to be able to facilitate the angiogenic process through VEGF secretion [39,40]. First, a wound healing test was used to assess the migration potential of HUVECs cultured in BMSC-CM derived from the coculturing of PT scaffolds and different concentrations of BMSCs. As displayed in Fig. 3A-O, the wound healing rate in the PT group was significantly lower than that in the other PT-BMSC groups at 12 h ($p < 0.05$), while there was no statistically

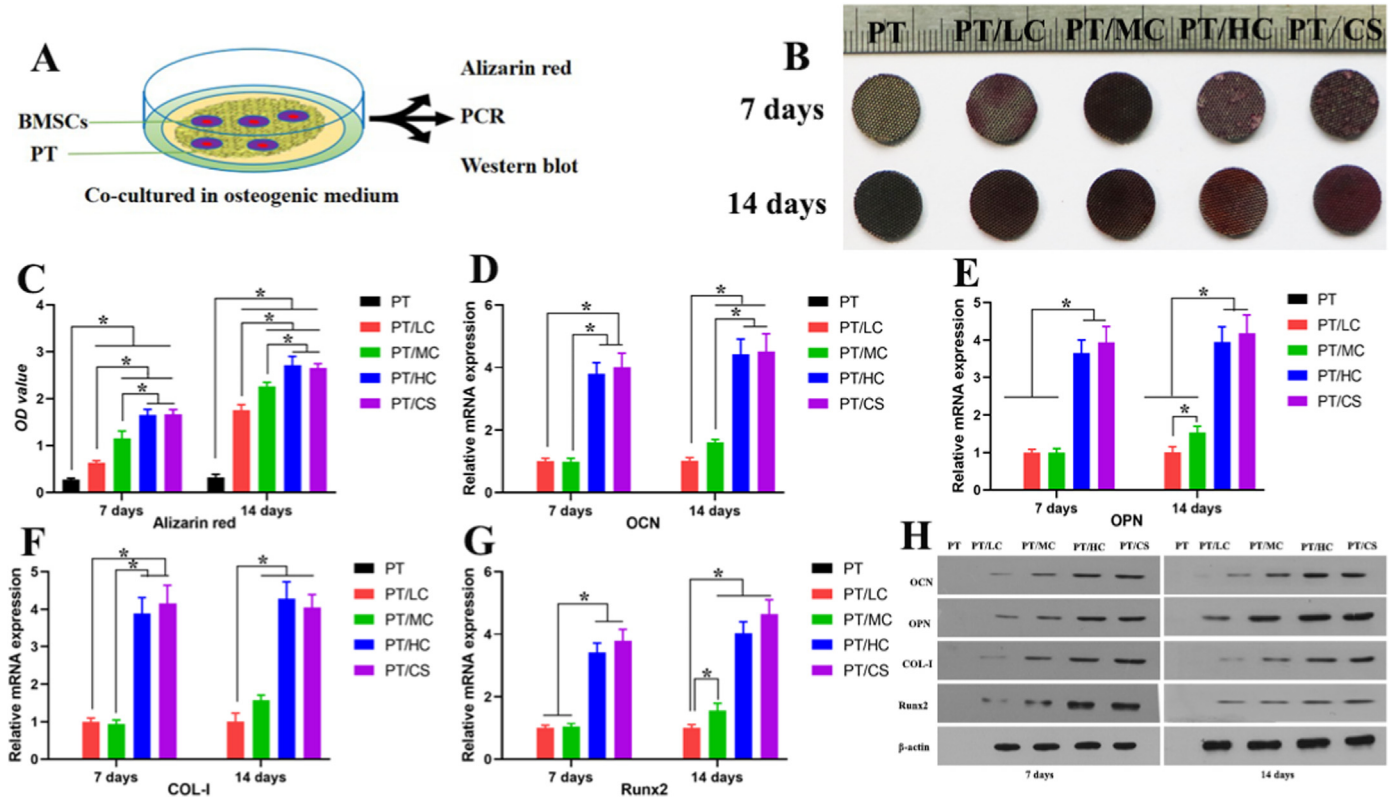

Fig. 2. In vitro analysis of osteogenesis of the combination of BMSCs and PT scaffolds. (A) Schematic of the experiment. BMSCs were collected from each group after 7 days and 14 days of coculturing with PT scaffolds in osteogenic induction medium. (B) Alizarin red staining images. (C) Quantification of Alizarin red staining based on the relative absorbance value. (D–G) The RT–PCR results of osteogenesis-related gene expression of OCN, OPN, COL-I, and Runx2 in the PT, PT/LC, PT/MC, PT/HC, and PT/CS groups on days 7 and 14. These results suggested that increasing the number of initial seeding cells improved the capability of osteogenic differentiation. (H) Western blot (WB) analysis presented results similar to those of RT–PCR. * indicates significant differences ($p < 0.05$).

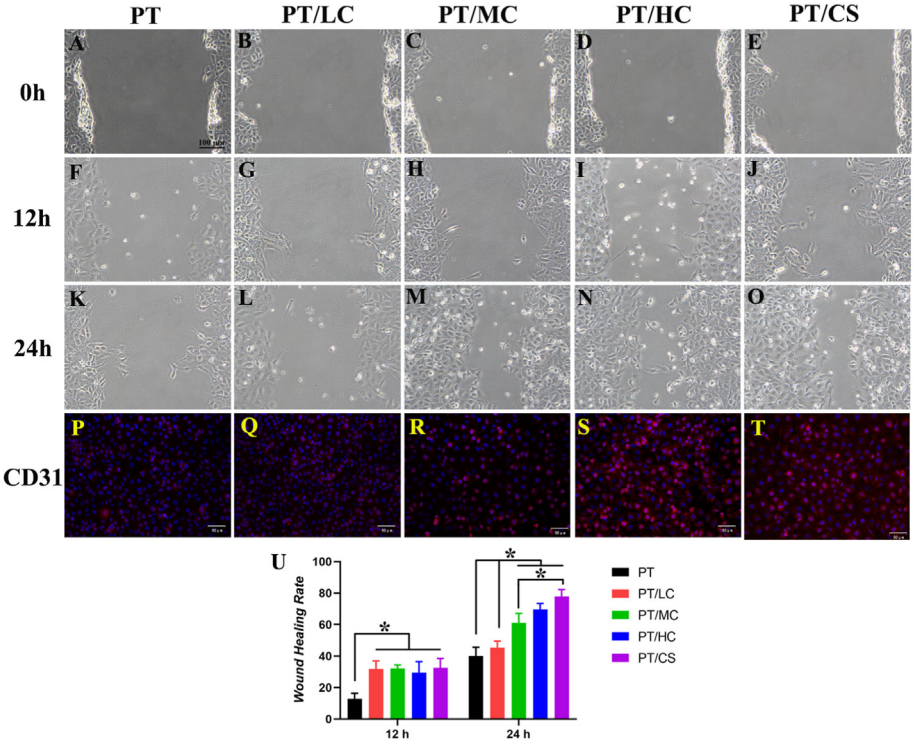

Fig. 3. The migration potential of HUVECs when cultured in BMSC-CM. (A–O) Wound healing assay results indicated that the more BMSCs were seeded, the faster the wound healed. Scale bar = 100 μm. (U) At 24 h, the wound healing rates in the PT and PT/LC groups were markedly lower than those in the other groups ($p < 0.05$), and there was no statistically significant difference between the PT/HC and PT/CS groups, which both had significantly higher rates than the PT/MC group. (P–T) Representative fluorescent images demonstrated that there were more CD31-positive cells in the PT/HC and PT/CS groups than in the other groups. Scale bar = 50 μm * indicates significant differences ($p < 0.05$).

significant difference between the PT/LC and PT/MC groups or the PT/HC and PT/CS groups ($p > 0.05$, Fig. 3U). After 24 h, the wound healing rates in the PT and PT/LC groups were markedly lower than those in the other groups ($p < 0.05$), and there was no statistically significant difference between the PT/HC and PT/CS groups, which both had significantly higher values than the PT/MC group ($p < 0.05$, Fig. 3U), indicating that the more BMSCs were seeded, the faster the wound healed. The good cytoskeleton observed in HUVECs indicated the cytocompatibility of PT scaffolds (Fig S5). Moreover, the representative fluorescent images demonstrated that there were more CD31-positive cells in the PT/HC and PT/CS groups than in the other groups (Fig. 3P-T). Then, the tube formation assay was used to verify angiogenesis with the combination of PT scaffolds and BMSCs. The tube formation results showed the formation of a capillary-like network with closed lumen morphology when HUVECs were cultured in BMSC-CM from the PT/HC and PT/CS groups, which led to a longer network of tube-like structures with more junctions than that in the other groups ($p < 0.05$, Fig. 4A-M). In addition, analyses of angiogenesis-related genes and proteins also confirmed the above results at the gene and protein levels. In detail, the mRNA expression levels of VEGF and bFGF, conventionally used as angiogenesis markers, were prominently upregulated in the PT/HC and PT/CS groups compared with the PT/MC group and were also significantly higher than those in the PT/LC and PT groups ($p < 0.05$, Fig. 4N and O). There was no significant difference between the PT and PT/LC groups ($p > 0.05$), indicating that the BMSCs have to reach a sufficient number to produce enough VEGF to promote angiogenesis [41]. In addition, the levels of VEGF and bFGF proteins were obviously higher in the PT/HC and PT/CS groups than in the other groups (Fig. 4P), which was consistent with the RT–PCR analysis results (Fig. 4N and O). Therefore, the PT/HC (seeding concentration at 5×10^5 cells/cm^2) and PT/CS (prepared osteogenic cell sheet wrapped PT scaffolds) groups were the best combination of BMSCs and PT scaffolds, producing the optimal outcomes for both osteogenesis and angiogenesis in vitro.

3.4. Evaluation of the effect of the combination of PT scaffolds and BMSCs on the construction of biomimetic engineered bone at an ectopic site

The PT/HC and PT/CS groups revealed more satisfactory osteogenesis and angiogenesis effects than the PT, PT/LC, and PT/MC groups in vitro. However, it remained unclear whether the PT/HC and PT/CS groups could achieve better bone regeneration in vivo. Therefore, a subcutaneous ectopic osteogenesis experiment was performed in nude mice to investigate the effects of bone regeneration in vivo, as shown in Fig. 5A–C. After 12 weeks of implantation, macroscopic views of the subcutaneous implantation sites revealed that the larger amount of ECM in osteoblastic BMSC sheets or produced during the coculturing of BMSCs and PT scaffolds in osteogenic medium markedly increased the

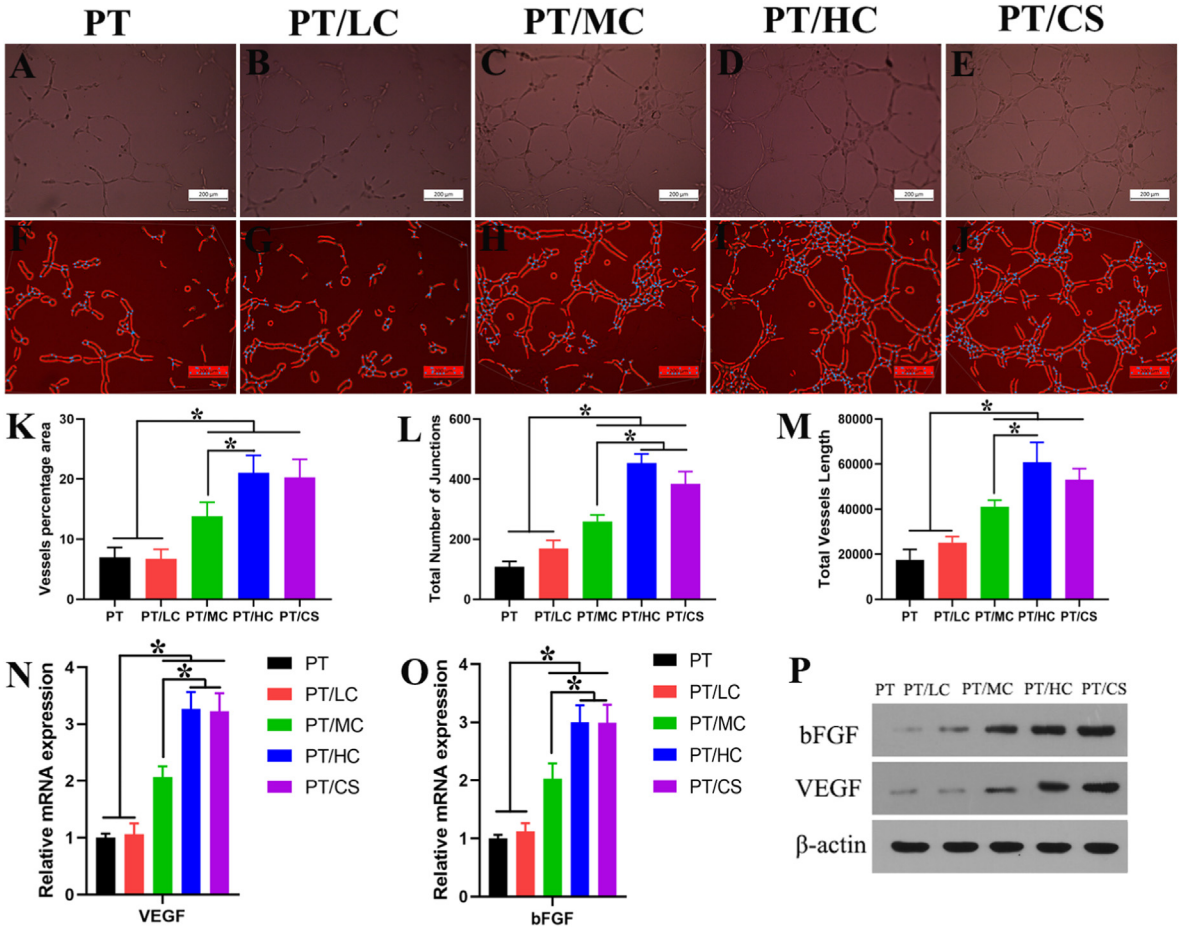

Fig. 4. In vitro analysis of angiogenesis of the combination of BMSCs and PT scaffolds. (A–E) A tube formation assay was used to verify angiogenesis with the combination of PT scaffolds and BMSCs. (F–M) Images were captured and analyzed quantitatively using AngioTool software. The tube formation results showed that a capillary-like network with closed lumen morphology formed when HUVECs were cultured in BMSC-CM from the PT/HC and PT/CS groups and led to a longer network of tube-like structures with more junctions than in the other groups. The vessel percentage area (K), total number of junctions (L), and total vessel length (M) were calculated based on AngioTool software to quantitatively compare tube formation among the different groups. (N and O) The RT–PCR results of angiogenesis-associated gene expression of VEGF and bFGF in the PT, PT/LC, PT/MC, PT/HC, and PT/CS groups. (P) WB analysis displayed results similar to those of RT–PCR. These results indicated that BMSCs have to reach a sufficient number to produce enough VEGF to promote angiogenesis. * indicates significant differences ($p < 0.05$).

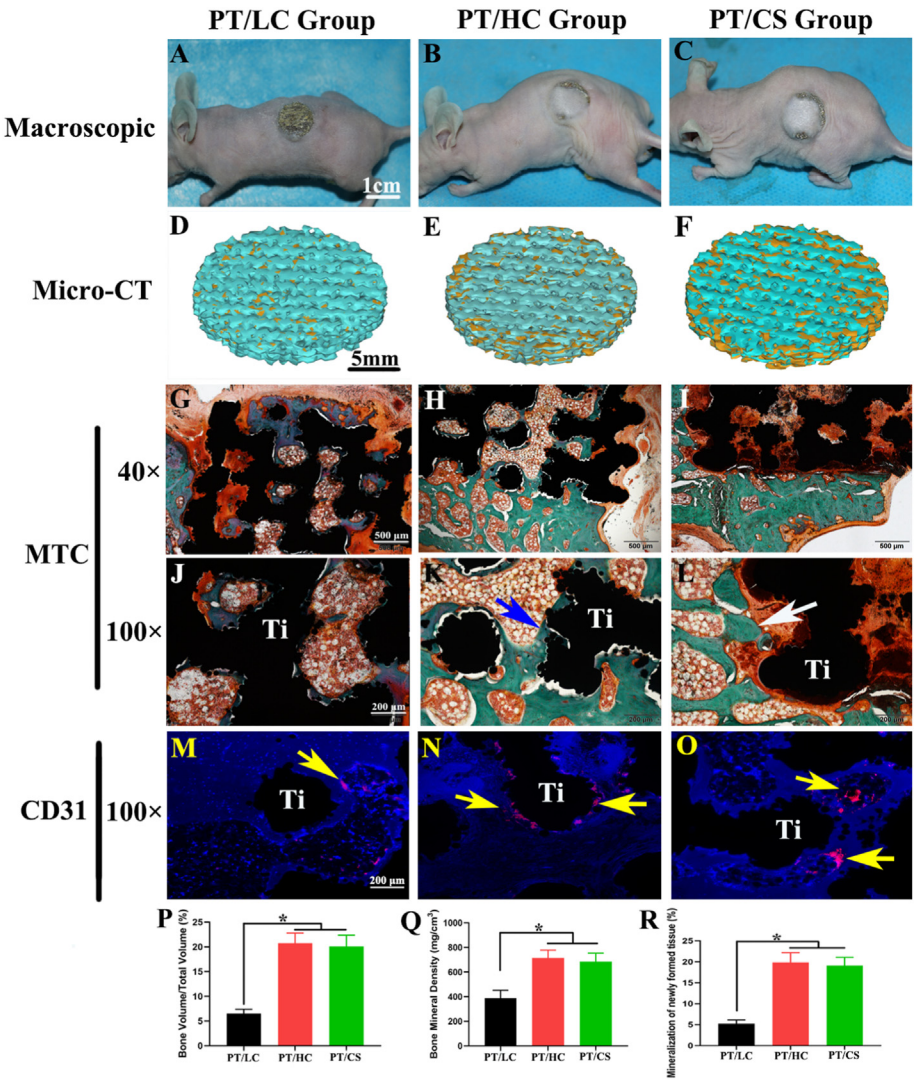

Fig. 5. Evaluation effect of the combination of PT scaffolds and BMSCs on the construction of biomimetic engineered bone at an ectopic site. (A–C) Macroscopic images of the subcutaneous implantation sites at 12 weeks of implantation. Scale bar = 1 cm. (D–F) Micro-CT reconstruction of the bone regeneration of the complex of PT scaffolds with BMSCs. The newly formed bones were brownish yellow in colour. (G–L) Masson's trichrome (MTC) staining of the PT scaffolds with BMSCs was performed to assess osteogenesis. Only a small quantity of regenerated bone was present in the PT/LC scaffolds (G and J), while more woven bone with more mature trabeculae was observed in the PT/HC (K, blue arrow) and PT/CS groups (L, white arrow). (G–I) Scale bar = 500 μm. (J–L) Scale bar = 200 μm. (M – O) CD31 immunofluorescence staining images of the newly formed vessels around PT scaffolds demonstrated that the newly formed vessels were more abundant in the PT/HC and PT/CS groups than in the PT/LC group (yellow arrow). Scale bar = 200 μm. (P) Bone volume/total volume (BV/TV) analysis of the complex of PT scaffolds with BMSCs at 12 weeks after implantation. (Q) Bone mineral density (BMD) analysis of the complex of PT scaffolds with BMSCs at 12 weeks after implantation. (R) Percentages of newly formed mineralized tissues among different groups. The percentages in the PT/HC and PT/CS groups were much greater than that in the PT/LC group. * indicates significant differences ($p < 0.05$).

biocompatibility of PT scaffolds and decreased the risk of metal exposure in PT/HC and PT/CS groups, which commonly occurs in patients who received titanium alloy plate for the immediate repair of postoperative defects after the removal of mandibular malignant tumors [42]. In contrast, the implanted PT scaffolds in the PT/LC group were almost completely exposed (Fig. 5A–C). Moreover, the ECM could mimic the microenvironment of the native ECM, which is beneficial for tissue development and organ formation [31]. The 3D reconstruction of micro-CT observations demonstrated that more newly regenerated bone formed in the PT/HC and PT/CS groups than in the PT/LC group (Fig. 5D–F). In detail, the ratio of newly formed bone volume and total tissue volume (BV/TV), regarded as the quantitative analysis index of regenerated bone, was measured based on the micro-CT scanning results. The BV/TV outcomes showed no significant difference between the PT/HC and PT/CS groups ($p > 0.05$, Fig. 5P), which both had significantly higher values than the PT/LC group ($p < 0.05$). In addition, bone mineral density (BMD), which reflects the osseointegration of newly formed bone, was also tested. Similar to the BV/TV results, a lower BMD level in the PT/LC group was present in the PT/HC and PT/CS groups ($p < 0.05$, Fig. 5Q). Combining the above results reveals that the addition of cell sheets consisting of ECM and BMSCs could increase the bone formation promoted by PT scaffolds in the PT/HC and PT/CS groups [28,43].

As displayed in Fig. 5G-L, the results of Masson's trichrome (MTC) staining encouraged the histological investigation of the osteogenic and angiogenic effects of the combinations of PT scaffolds and cell sheet technology. On week 12, only a small quantity of regenerated bone was present in the PT/LC scaffolds, while more woven bone with more mature trabeculae was observed in the PT/HC and PT/CS groups (Fig. 5K and L, blue arrow and white arrow, respectively), which was verified by histomorphometric examinations ($p < 0.05$, Fig. 5L) and was in accordance with the results of OCN immunostaining, a specific marker of osteoblastic differentiation of the BMSCs (Fig S6). Specifically, newly regenerated bone was found around the PT scaffolds in the PT/HC group (Fig. 5K, blue arrow), indicating that the coculturing of BMSCs and PT scaffolds allowed the deposition of osteoblastic matrix on the surface of the scaffolds, which was consistent with the SEM observation results (Fig. 1S, blue arrow). Moreover, there was more bone formation around the scaffold than inside the scaffold (Fig. 5H, I, K, and L), suggesting that regenerated bone was first formed on the surface of the scaffold and then grew inward and occupied the pores of the scaffold, which was consistent with previously reported results [7,28]. This phenomenon may be attributed to the sufficient nutrition supply around the scaffold in the early stage of bone formation and the effective nutrition communication within the porous scaffold in the later stage of bone regeneration and remodeling, which combine to result in incremental bone ingrowth [7,28,44]. At the same time, histological observations of the main organs, including heart, liver, spleen, lung, and kidney tissues, demonstrated that there was no obvious difference between the PT group and the normal group (Fig S7A-T), which indicated the biosafety and biocompatibility of

PT scaffolds in vivo [28].

Angiogenesis is vital for bone regeneration and remodeling because it enables adequate nutrition supply and communication [41]. CD31, regarded as a biomarker of endothelial cells, was tested to investigate the angiogenesis of the scaffolds. The results of immunofluorescence CD31 staining indicated more newly formed vessels in the PT/HC and PT/CS groups than in the PT/LC group (Fig. 5M – O, yellow arrow). Taken together, the interaction between implanted BMSCs and ECM existed in osteoblastic BMSC sheets or was produced during the coculturing of BMSCs and PT scaffolds in osteogenic medium, resulting in VEGF production (Fig. 4N and P, Fig S8), which is believed to recruit vasculogenic cells and facilitate the migration of HUVECs (Fig. 3A-O) [40,41,45]. In addition, the presence of VEGF could recruit more MSCs, including BMSCs and hematopoietic stem cells; increase vessel tube formation (Fig. 4A-M); and facilitate the establishment of capillary networks (Fig. 5N and O), thus facilitating cell sheet remodeling as well as bone regeneration in PT scaffolds [46]. Furthermore, the abundant intercommunication porous structures of PT scaffolds provided suitable channels and environments for the ingrowth of cells and blood vessels [29], and the good biomechanical properties of the PT scaffolds provided indispensable mechanical support for the remodeling and maturation of regenerated bone tissues [25].

Although our results confirm that the fabrication of engineered bone tissue based on 3D printed PT scaffolds combined with osteoblastic BMSC sheets at an ectopic site within 12 weeks after implantation, this study remains several limitations. For example, experiments testing the ability of this composite constructs to repair bone defects in an animal model, such as radius defect rabbit model, should be carried out, because our present study only tested the ectopic osteogenesis of PT-BMSCs sheet composite in SCID mice. Furthermore, the potential molecular mechanisms responsible for the increase in the osteogenic potential of the combination of PT scaffolds and BMSC sheet technology should also be studied in the future.

In brief, the in vivo results were in line with the in vitro results, indicating that the combination of PT scaffolds and BMSC sheet technology could significantly improve osteogenesis and angiogenesis, and the PT/HC and PT/CS groups displayed the best effects with no significant difference.

4. Conclusion

In summary, 3D-printed PT was combined with a BMSC sheet to develop a hybrid scaffold with ideal mechanical features, customizability, and bionic characteristics for the construction of biomimetic engineered bone at an ectopic site. In our study, BMSCs cultured to form osteoblastic cell sheets or cocultured with PT scaffolds secreted ECM, mimicking the microenvironment of native ECM, while 3D-printed PT was used to mimic the microstructure and mechanical features of native bone. The addition of BMSCs and their self-secreted osteoblastic ECM to PT scaffolds significantly enhanced osteogenesis and angiogenesis in vitro and in vivo compared to the performance of PT scaffold grafts alone. Moreover, the PT/HC (seeding concentration at 5×10^5 cells/cm^2) and PT/CS (prepared osteogenic cell sheet-wrapped PT scaffolds) groups exhibited the best osteogenic and angiogenic effects with no significant difference between them. The potential mechanisms of these effects may be attributed to the 3D microstructure of PT scaffolds facilitating the biological behaviors of cells and to the presence of BMSCs and ECM increasing the osteogenic and angiogenic potential of PT scaffolds by providing stem cells and secreting VEGF. Therefore, the combination of BMSC sheet technology and 3D PT scaffolds could be used to construct customized biomimetic engineered bone, thus offering a novel and promising strategy for the precise repair of bone defects.

Consent for publication

All authors have read and approved the content and agreed to submit this manuscript to be considered for publication in the journal.

Credit author statement

Zhifa Wang: Methodology, Investigation, Data curation, Formal analysis, Funding acquisition, Writing – original draft.**Leng Han**: Methodology, Investigation, Data curation, Formal analysis, Writing – original draft. **Ye Zhou**: Methodology, Investigation, Data curation, Formal analysis, Writing – original draft.**Jiacheng Cai**: Investigation, Validation, Methodology.**Shuohui Sun**: Investigation, Formal analysis.**Junli Ma**: Data curation, Methodology, Formal analysis.**Weijian Wang**: Methodology, Project administration, Supervision. **Xiao Li**: Methodology, Project administration, Supervision.**Limin Ma**: Methodology, Project administration, Supervision, Funding acquisition, Writing – review & editing.

Declaration of competing interest

The authors declare that they have no known competing financial interests or personal relationships that could have appeared to influence the work reported in this paper.

Data availability

Data will be made available on request.

Acknowledgments

This study was funded by the Military Medical Technology Youth Cultivation Project of PLA (20QNPY081), China, the Military Logistic Science Research Project of PLA (BGZ15J001), China, the National Natural Science Foundation of China (81700943), the Natural Science Foundation of Guangdong Province (2017A030310671), China, the Science and Technology Planning Project of Guangzhou City, China (202102021269), and the Highlevel Hospital Construction Project of Guangdong Provincial People's Hospital (KJ012019100), China.

Appendix A. Supplementary data

Supplementary data to this article can be found online at https://doi.org/10.1016/j.mtbio.2022.100433.

References

[1] E. Ruales-Carrera, M. Engler, P. Vaz, M. Ozcan, C.A.M. Volpato, Esthetic and functional rehabilitation of bilateral congenital absence of maxillary lateral incisors: minimally invasive surgical and prosthetic approach, J. Esthetic Restor. Dent. 31 (1) (2019) 5–12.

[2] Z. Wang, Y. Weng, S. Lu, C. Zong, J. Qiu, Y. Liu, et al., Osteoblastic mesenchymal stem cell sheet combined with Choukroun platelet-rich fibrin induces bone formation at an ectopic site, J. Biomed. Mater. Res. B Appl. Biomater. 103 (6) (2015) 1204–1216.

[3] J. Biggemann, M. Pezoldt, M. Stumpf, P. Greil, T. Fey, Modular ceramic scaffolds for individual implants, Acta Biomater. 80 (2018) 390–400.

[4] Q. Sun, Z. Li, B. Liu, X. Yuan, S. Guo, J.A. Helms, Improving intraoperative storage conditions for autologous bone grafts: an experimental investigation in mice, J Tissue Eng Regen Med 13 (12) (2019) 2169–2180.

[5] R. Ikeguchi, T. Aoyama, R. Kakinoki, M. Ueda, Y. Kasai, T. Maekawa, et al., A clinical trial for Kienbock disease by cultured autologous multipotent mesenchymal stromal cells augmented with vascularized bone grafts: a report of five cases, J. Orthop. Sci. 24 (4) (2019) 750–756.

[6] C.X. Mae, N.Y. Shetty, P.G. Patil, Radiographic evaluation of crestal bone level changes for allografts or xenografts placed during implant placement: a retrospective study, J. Contemp. Dent. Pract. 22 (10) (2021) 1082–1086.

[7] S.T. Ildstad, D.H. Sachs, Reconstitution with syngeneic plus allogeneic or xenogeneic bone marrow leads to specific acceptance of allografts or xenografts, Nature 307 (5947) (1984) 168–170.
[8] D.M. Lough, C. Chambers, G. Germann, R. Bueno, J. Reichensperger, E. Swanson, et al., Regulation of adsc osteoinductive potential using notch pathway inhibition and gene rescue: a potential on/off switch for clinical applications in bone formation and reconstructive efforts, Plast. Reconstr. Surg. 138 (4) (2016) 642e–652e.
[9] M. Sadat-Ali, D.A. Al-Dakheel, A. Ahmed, H.A. Al-Turki, A.S. Al-Omran, S. Acharya, et al., Spinal cord injury regeneration using autologous bone marrow-derived neurocytes and rat embryonic stem cells: a comparative study in rats, World J. Stem Cell. 12 (12) (2020) 1591–1602.
[10] M. Emadedin, N. Labibzadeh, R. Fazeli, F. Mohseni, S.E. Hosseini, R. Moghadasali, et al., Percutaneous autologous bone marrow-derived mesenchymal stromal cell implantation is safe for reconstruction of human lower limb long bone atrophic nonunion, Cell J 19 (1) (2017) 159–165.
[11] D. Ma, C. Zhong, H. Yao, Y. Liu, F. Chen, J. Li, et al., Engineering injectable bone using bone marrow stromal cell aggregates, Stem Cell. Dev. 20 (6) (2011) 989–999.
[12] G.S. Krishnakumar, S. Sampath, S. Muthusamy, M.A. John, Importance of crosslinking strategies in designing smart biomaterials for bone tissue engineering: a systematic review, Mater Sci Eng C Mater Biol Appl 96 (2019) 941–954.
[13] D. Khare, B. Basu, A.K. Dubey, Electrical stimulation and piezoelectric biomaterials for bone tissue engineering applications, Biomaterials 258 (2020), 120280.
[14] T. Winkler, F.A. Sass, G.N. Duda, K. Schmidt-Bleek, A review of biomaterials in bone defect healing, remaining shortcomings and future opportunities for bone tissue engineering: the unsolved challenge, Bone Joint Res 7 (3) (2018) 232–243.
[15] I. Elloumi-Hannachi, M. Yamato, T. Okano, Cell sheet engineering: a unique nanotechnology for scaffold-free tissue reconstruction with clinical applications in regenerative medicine, J. Intern. Med. 267 (1) (2010) 54–70.
[16] K. Ohashi, T. Yokoyama, M. Yamato, H. Kuge, H. Kanehiro, M. Tsutsumi, et al., Engineering functional two- and three-dimensional liver systems in vivo using hepatic tissue sheets, Nat Med 13 (7) (2007) 880–885.
[17] T. Shimizu, H. Sekine, J. Yang, Y. Isoi, M. Yamato, A. Kikuchi, et al., Polysurgery of cell sheet grafts overcomes diffusion limits to produce thick, vascularized myocardial tissues, Faseb. J. 20 (6) (2006) 708–710.
[18] Y.Y. Gong, J.X. Xue, W.J. Zhang, G.D. Zhou, W. Liu, Y. Cao, A sandwich model for engineering cartilage with acellular cartilage sheets and chondrocytes, Biomaterials 32 (9) (2011) 2265–2273.
[19] H. Zhang, Y. Zhou, W. Zhang, K. Wang, L. Xu, H. Ma, et al., Construction of vascularized tissue-engineered bone with a double-cell sheet complex, Acta Biomater. 77 (2018) 212–227.
[20] S. Barui, A.K. Panda, S. Naskar, R. Kuppuraj, S. Basu, B. Basu, 3D inkjet printing of biomaterials with strength reliability and cytocompatibility: quantitative process strategy for Ti-6Al-4V, Biomaterials 213 (2019), 119212.
[21] L. Ma, X. Wang, N. Zhao, Y. Zhu, Z. Qiu, Q. Li, et al., Integrating 3D printing and biomimetic mineralization for personalized enhanced osteogenesis, angiogenesis, and osteointegration, ACS Appl. Mater. Interfaces 10 (49) (2018) 42146–42154.
[22] A. Ravida, R. Siqueira, I. Saleh, M.H.A. Saleh, A. Giannobile, H.L. Wang, Lack of clinical benefit of implantoplasty to improve implant survival rate, J. Dent. Res. 99 (12) (2020) 1348–1355.
[23] S. Mei, H. Wang, W. Wang, L. Tong, H. Pan, C. Ruan, Q. Ma, et al., Antibacterial effects and biocompatibility of titanium surfaces with graded silver incorporation in titania nanotubes, Biomaterials 35 (14) (2014) 4255–4265.
[24] P. Xiu, Z. Jia, J. Lv, C. Yin, Y. Cheng, K. Zhang, et al., Tailored surface treatment of 3D printed porous Ti6Al4V by microarc oxidation for enhanced osseointegration via optimized bone in-growth patterns and interlocked bone/implant interface, ACS Appl. Mater. Interfaces 8 (28) (2016) 17964–17975.
[25] P. Gao, B. Fan, X. Yu, W. Liu, J. Wu, L. Shi, et al., Biofunctional magnesium coated Ti6Al4V scaffold enhances osteogenesis and angiogenesis in vitro and in vivo for orthopedic application, Bioact. Mater. 5 (3) (2020) 680–693.
[26] S.Y. He, Y. Zhang, Y. Zhou, N. Bao, Y. Cai, P. Zhou, et al., Modeling osteoinduction in titanium bone scaffold with a representative channel structure, Mater Sci Eng C Mater Biol Appl 117 (2020), 111347.
[27] C. McBeth, J. Lauer, M. Ottersbach, J. Campbell, A. Sharon, A.F. Sauer-Budge, 3D bioprinting of GelMA scaffolds triggers mineral deposition by primary human osteoblasts, Biofabrication 9 (1) (2017), 015009.
[28] L. Ma, X. Wang, Y. Zhou, X. Ji, S. Cheng, D. Bian, et al., Biomimetic Ti-6Al-4V alloy/gelatin methacrylate hybrid scaffold with enhanced osteogenic and angiogenic capabilities for large bone defect restoration, Bioact. Mater. 6 (10) (2021) 3437–3448.
[29] C. Torres-Sanchez, F.R.A. Al Mushref, M. Norrito, K. Yendall, Y. Liu, P.P. Conway, The effect of pore size and porosity on mechanical properties and biological response of porous titanium scaffolds, Mater Sci Eng C Mater Biol Appl 77 (2017) 219–228.
[30] K.E. Benders, P.R. van Weeren, S.F. Badylak, D.B. Saris, W.J. Dhert, J. Malda, Extracellular matrix scaffolds for cartilage and bone regeneration, Trends Biotechnol. 31 (3) (2013) 169–176.
[31] E. Vorotnikova, D. McIntosh, A. Dewilde, J. Zhang, J.E. Reing, L. Zhang, et al., Extracellular matrix-derived products modulate endothelial and progenitor cell migration and proliferation in vitro and stimulate regenerative healing in vivo, Matrix Biol. 29 (8) (2010) 690–700.
[32] Z. Wang, Z. Li, Z. Li, B. Wu, Y. Liu, W. Wu, Cartilaginous extracellular matrix derived from decellularized chondrocyte sheets for the reconstruction of osteochondral defects in rabbits, Acta Biomater. 81 (2018) 129–145.
[33] Z. Wang, L. Han, T. Sun, J. Ma, S. Sun, L. Ma, et al., Extracellular matrix derived from allogenic decellularized bone marrow mesenchymal stem cell sheets for the reconstruction of osteochondral defects in rabbits, Acta Biomater. 118 (2020) 54–68.
[34] J. Park, J. Lee, J. Kwag, Y. Baek, B. Kim, C.J. Yoon, et al., Quantum dots in an amphiphilic polyethyleneimine derivative platform for cellular labeling, targeting, gene delivery, and ratiometric oxygen sensing, ACS Nano 9 (6) (2015) 6511–6521.
[35] C. Ning, P. Yu, Y. Zhu, M. Yao, X. Zhu, X. Wang, et al., Built-in microscale electrostatic fields induced by anatase-rutile-phase transition in selective areas promote osteogenesis, NPG Asia Mater. 8 (2016).
[36] X. Xie, P. Qu, H. Wu, P. Liu, J. Luo, J. Chi, et al., Circulating exosomal miR-21 mediates HUVEC proliferation and migration through PTEN/PI3K/AKT in Crohn's disease, Ann. Transl. Med. 10 (5) (2022) 258.
[37] X. Fang, J. Xie, L. Zhong, J. Li, D. Rong, X. Li, et al., Biomimetic gelatin methacrylamide hydrogel scaffolds for bone tissue engineering, J. Mater. Chem. B 4 (6) (2016) 1070–1080.
[38] K. Hu, B.R. Olsen, Osteoblast-derived VEGF regulates osteoblast differentiation and bone formation during bone repair, J. Clin. Invest. 126 (2) (2016) 509–526.
[39] A.A. Kocher, M.D. Schuster, M.J. Szabolcs, S. Takuma, D. Burkhoff, J. Wang, et al., Neovascularization of ischemic myocardium by human bone-marrow-derived angioblasts prevents cardiomyocyte apoptosis, reduces remodeling and improves cardiac function, Nat Med 7 (4) (2001) 430–436.
[40] R. Ba, J. Wei, M. Li, X. Cheng, Y. Zhao, W. Wu, Cell-bricks based injectable niche guided persistent ectopic chondrogenesis of bone marrow-derived mesenchymal stem cells and enabled nasal augmentation, Stem Cell Res. Ther. 6 (2015) 16.
[41] Z. Li, R. Ba, Z. Wang, J. Wei, Y. Zhao, W. Wu, Angiogenic potential of human bone marrow-derived mesenchymal stem cells in chondrocyte brick-enriched constructs promoted stable regeneration of craniofacial cartilage, Stem Cells Transl Med 6 (2) (2017) 601–612.
[42] H. Hirohata, T. Yanagawa, S. Takaoka, K. Yamagata, K. Sasaki, Y. Shibuya, et al., A small number of residual teeth after the mandibular resection of oral cancer is associated with titanium reconstruction plate exposure, Clin Exp Dent Res 5 (5) (2019) 469–475.
[43] Z. Zhao, S. Ma, C. Wu, X. Li, X. Ma, H. Hu, et al., Chimeric peptides quickly modify the surface of personalized 3D printing titanium implants to promote osseointegration, ACS Appl. Mater. Interfaces 13 (29) (2021) 33981–33994.
[44] Y. Zhang, N. Sun, M. Zhu, Q. Qiu, P. Zhao, C. Zheng, et al., The contribution of pore size and porosity of 3D printed porous titanium scaffolds to osteogenesis, Mater Sci Eng C Mater Biol Appl (2022), 112651.
[45] B.N. Brown, S.F. Badylak, Extracellular matrix as an inductive scaffold for functional tissue reconstruction, Transl. Res. 163 (4) (2014) 268–285.
[46] H. Zhang, Y. Zhou, N. Yu, H. Ma, K. Wang, J. Liu, et al., Construction of vascularized tissue-engineered bone with polylysine-modified coral hydroxyapatite and a double cell-sheet complex to repair a large radius bone defect in rabbits, Acta Biomater. 91 (2019) 82–98.